

Article

In Situ Synthesis of Bi₂S₃/BiFeO₃ Nanoflower Hybrid Photocatalyst for Enhanced Photocatalytic Degradation of Organic Pollutants

Rentao Zhou¹, Xinman Tu^{1,2,*}, Peng Zheng², Li Zhang²  and Zhenxing Zeng^{3,*}¹ College of Environment Science and Engineering, Guilin University of Technology, Guilin 541004, China² Key Laboratory of Jiangxi Province for Persistent Pollutants Control and Resources Recycle, Nanchang Hangkong University, Nanchang 330063, China; 17770042612@163.com (P.Z.)³ College of Environmental Sciences, Sichuan Agricultural University, Chengdu 611130, China

* Correspondence: tuxinman@126.com (X.T.); zxzeng@sicau.edu.cn (Z.Z.)

Abstract: Photocatalytic degradation of Malachite Green oxalate (MG) in a water body is of significant importance to our health protection, as it could cause various serious diseases. However the photocatalytic activity of most catalysts is still unsatisfactory, due to the poor reactive oxygen species production as a result of sluggish charge separation. Here, innovative nanoflower-shaped Bi₂S₃/BiFeO₃ heterojunctions are prepared via a facile sol–gel method, exhibiting an enhanced reactive oxygen species generation, which leads to the excellent photocatalytic performance toward MG degradation. We verify that interfacing BiFeO₃ with Bi₂S₃ could form a fine junction and offers a built-in field to speed up charge separation at the junction area; as a result, this shows much higher charge separation efficiency. By virtue of the aforementioned advantages, the as-prepared Bi₂S₃/BiFeO₃ heterojunctions exhibit excellent photocatalytic performance toward MG degradation, where more than 99% of MG is removed within 2 h of photocatalysis. The innovative design of nanoflower-like Bi₂S₃/BiFeO₃ heterojunctions may offer new viewpoints in designing highly efficient photocatalysts for environmentally related applications.

Keywords: photocatalysis; advanced oxidation processes; organic degradation; heterojunction

Citation: Zhou, R.; Tu, X.; Zheng, P.; Zhang, L.; Zeng, Z. In Situ Synthesis of Bi₂S₃/BiFeO₃ Nanoflower Hybrid Photocatalyst for Enhanced Photocatalytic Degradation of Organic Pollutants. *Molecules* **2023**, *28*, 8007. <https://doi.org/10.3390/molecules28248007>

Academic Editors: Ying Zhang and Fangke Yu

Received: 16 October 2023

Revised: 29 November 2023

Accepted: 30 November 2023

Published: 8 December 2023



Copyright: © 2023 by the authors. Licensee MDPI, Basel, Switzerland. This article is an open access article distributed under the terms and conditions of the Creative Commons Attribution (CC BY) license (<https://creativecommons.org/licenses/by/4.0/>).

1. Introduction

In recent years, the world has been grappling with escalating energy crises and environmental pollution issues, particularly the pervasive presence of organic pollutants that significantly affect people's daily lives. As the organic pollutants in water bodies are mostly highly toxic and may cause various serious diseases, effectively eliminating harmful organic pollutants from the environment has become a paramount concern for the scientific community. As a safe and sustainable way for organic pollutant removal, photocatalytic degradation of organics following a radical oxidative manner in recent years has been intensively studied. The key to achieving highly efficient organic pollutant removal from a water body lies in the development of a cost-effective photocatalyst with high reactive radical generation efficiency [1,2]. Unfortunately, most widely used photocatalysts primarily respond to UV–visible irradiation, limiting their practicality under visible light. Consequently, the quest for highly efficient and stable visible-light-driven photocatalysts has emerged as a hot topic in the field of photocatalysis.

Recently, BiFeO₃ photocatalysts have garnered attention, due to their lower energy bandgap, excellent chemical stability at room temperature, and superior carrier transport properties. BiFeO₃ holds promise for catalytic applications under visible light. Research has shown that BiFeO₃, with a bandgap of approximately 2.2 eV [3,4], exhibits a favorable response to visible light and has been employed for the optical degradation of organic pollutants in water, including the degradation of organic dyes [5–13]. To further enhance

the photocatalytic activity of BiFeO₃, researchers have explored various modification techniques. Common approaches include element doping [14–16], which can boost visible-light-driven photocatalytic activity but often fails to effectively suppress the recombination of photogenerated electron–hole pairs, resulting in limited solar energy utilization. Some scholars have also experimented with noble metal deposition methods [17,18]; however, the high cost of precious metals makes these approaches less practical for real-world applications. Additionally, these modifications require further optimization to achieve better responsiveness to the visible light spectrum. As a result, researchers have turned to the incorporation of various materials into BiFeO₃ to form composite heterojunction structures, such as CuO [19], TiO₂ [20,21], and graphene oxide (GO) [22,23], among others. These heterojunction structures have been effective in enhancing visible light photocatalytic activity by mitigating electron–hole-pair recombination. However, these heterojunctions still lack optimal reducibility and oxidizability for photogenerated electron–hole pairs.

Hence, the search for a new semiconductor material to create heterojunctions with stronger reducibility and oxidizability is imperative. Additionally, since BiFeO₃ nanoparticles possess a limited specific surface area, finding a substance capable of effectively increasing its surface area is crucial for enhancing photocatalytic reactions. Based on these considerations, our research aims to improve the reducibility and oxidizability of BiFeO₃ through the formation of heterojunction structures with other materials, while simultaneously increasing its surface area. Achieving this under economical, simple, and mild reaction conditions has been a primary objective in our field. Our investigation revealed that Bi₂S₃, with its narrow band gap ($E_g = 1.38\text{--}1.71$ eV) [24] and the ability to adjust heterojunction morphology, is an ideal material for combining with BiFeO₃. While previous studies have explored the potential of Bi₂S₃ as a visible-light-driven photocatalyst in conjunction with other photocatalysts, such as BiOCl [25,26], ZnO [27], TiO₂ [28], CdS [29], WO₃ [30], BiFeO₃/ α -Fe₂O₃ [31], La_xBa_{1-x}Sr_yCd_{1-y}O_{3± δ} [32], Bi₂WO₆ [33], BiVO₄ [34], and Bi₂O₃ [35], no reports exist on the Bi₂S₃/BiFeO₃ heterojunction photocatalysis.

In this study, we employed the in situ growth method to synthesize a novel Bi₂S₃/BiFeO₃ nanoflower structure, demonstrating enhanced photocatalytic performance under visible light irradiation. We employed MG as a model contaminant to evaluate the material's efficiency. Furthermore, we comprehensively investigated the structure, composition, morphology, and mechanism of this novel photocatalyst.

2. Results and Discussion

Figure 1 displays the X-ray diffraction (XRD) patterns of the Bi₂S₃/BiFeO₃ samples with varying molar mass ratios, ranging from 1:2 to 1:4, in addition to pure BiFeO₃, for comparison. The XRD patterns of pure BiFeO₃ align well with the JCPDS 20-0169 standard [36], indicating the presence of characteristic diffraction peaks associated with this compound. In the composite material, discernible diffraction peaks attributed to Bi₂S₃ are evident, indicating the successful incorporation of Bi₂S₃ into the structure. It is worth noting that the diffraction peak of Bi₂S₃ at $2\theta = 25.32$ exhibits a slight overlap with BiFeO₃ ($2\theta = 25.40$). A noteworthy observation is that the positions of the Bi₂S₃ diffraction peaks at 25.2 and 28.6 display minor shifts towards larger angles in the composite material. These shifts suggest that Bi₂S₃ has effectively integrated with BiFeO₃, leading to a reduction in the crystalline lattice spacing. Furthermore, it is important to acknowledge that the crystallinity of Bi₂S₃, synthesized via a hydrothermal method, is comparatively inferior to that of BiFeO₃. These XRD findings shed light on the successful synthesis of Bi₂S₃/BiFeO₃ composites and the structural modifications induced by their integration.

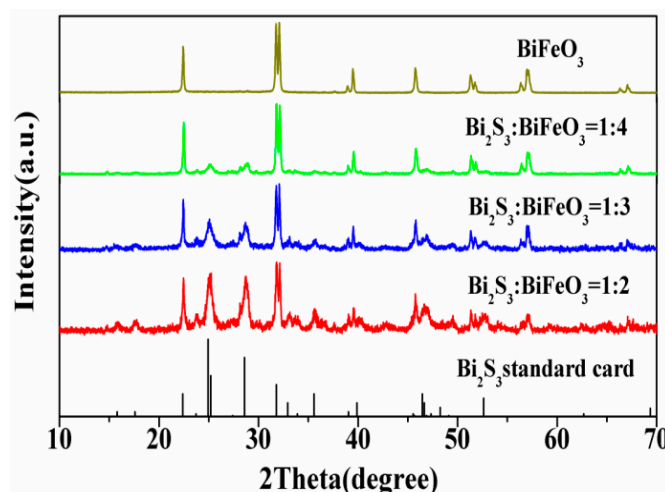


Figure 1. XRD patterns of $\text{Bi}_2\text{S}_3/\text{BiFeO}_3$ with different proportions.

The microcosmic morphologies and microstructure of both pure BiFeO_3 and $\text{Bi}_2\text{S}_3/\text{BiFeO}_3$ were meticulously examined using SEM, TEM, and HRTEM, revealing intriguing insights. SEM images of pure BiFeO_3 , as shown in Figure 2a, depict an assembly of particles characterized by smooth borderlines. However, the introduction of sulfur for the ion exchange process brought about significant changes in the morphology of the composite materials. As evidenced in Figure 2d, there is a noticeable shift towards a nearly spherical flower-like shape. Detailed TEM analysis, displayed in Figure 2e, unequivocally indicates the growth of Bi_2S_3 on the surface of BiFeO_3 through ion exchange. HRTEM provided further elucidation, revealing that Bi_2S_3 exposes more planes corresponding to crystal planes (310) and (211), which correspond to lattice spacings of 0.3530 nm and 0.3120 nm, respectively. The formation mechanism of these changes can be understood as follows: Initially, the lattice of BiFeO_3 is pristine, with filled bonding orbitals and relatively few dangling bonds at the interface, rendering the entire BiFeO_3 molecule in a stable state. The introduction of sulfuric acid provides the necessary energy for the surface activation of BiFeO_3 . This activation leads to damage to the original crystal lattice, exposing elemental bismuth and creating an abundance of dangling bonds on the surface of BiFeO_3 . Consequently, surface energy increases significantly, enhancing surface activity. When L-cysteine is introduced, a critical chemical transformation occurs. The elemental sulfur in L-cysteine forms stable new chemical bonds with the elemental bismuth on the surface of BiFeO_3 , resulting in the formation of $\text{Bi}_2\text{S}_3/\text{BiFeO}_3$ heterojunctions. Moreover, the EDX spectrum analysis corroborates these findings, as it reveals the presence of Bi, O, Fe, and S elements, further confirming the formation mechanism of the $\text{Bi}_2\text{S}_3/\text{BiFeO}_3$ heterojunction.

To gain further insight into the surface composition of the heterojunction material, X-ray photoelectron spectroscopy (XPS) was employed, providing compelling evidence for the coexistence of Bi_2S_3 and BiFeO_3 , as well as the presence of Bi, Fe, O, and S elements (Figure 3). The high-resolution XPS spectra reveal overlapping peaks centered at 158.2 eV and 163.6 eV, as well as 159.2 eV and 164.5 eV. These peaks can be attributed to the binding energy of $\text{Bi}^{3+} 4f_{7/2}$ and $4f_{5/2}$ in Bi_2S_3 [28] and the Bi-O bond in BiFeO_3 [37,38], respectively. The XPS spectrum of Fe(2p) is noteworthy, exhibiting six peaks at 709.9, 711.3, 715.5, 719.0, 723.4, and 725.0 eV. Notably, the Fe(2p) peaks at binding energies of 711.3/725.0 eV and 709.9/723.4 eV, along with a satellite signal peak at 719.0 eV and 715.5 eV, are characteristic of Fe^{3+} and Fe^{2+} . The Fe(2p) spectra primarily feature two maxima peaks corresponding to the electron levels of $\text{Fe} 2p_{3/2}$ and $\text{Fe} 2p_{1/2}$ [39,40]. It is worth noting that the peak of the high-spin Fe^{3+} ion is significantly broader, compared to the low-spin Fe^{2+} ions. This broadening can be attributed to electrostatic interactions and spin-orbit coupling among the 2p empty orbital and the unpaired 3d electrons of iron ions. In the XPS spectrum of O 1s, four distinct peaks were observed at 529.3, 530.8, 532.2, and 533.2 eV, corresponding

to oxygen–metal bonds in the lattice O_2^- of $BiFeO_3$ [41], remaining OH^- at the material surface [42], adsorbed oxygen (O_{ads}), and surface-adsorbed H_2O [43]. The presence of a smaller-intensity peak at a binding energy of 225.4 eV in the S 2s spectrum can be attributed to the S–Bi bond of Bi_2S_3 [44]. In conclusion, the XPS analysis unequivocally confirms the successful growth of Bi_2S_3 nanomaterials on the surface of $BiFeO_3$, forming the $Bi_2S_3/BiFeO_3$ heterojunction.

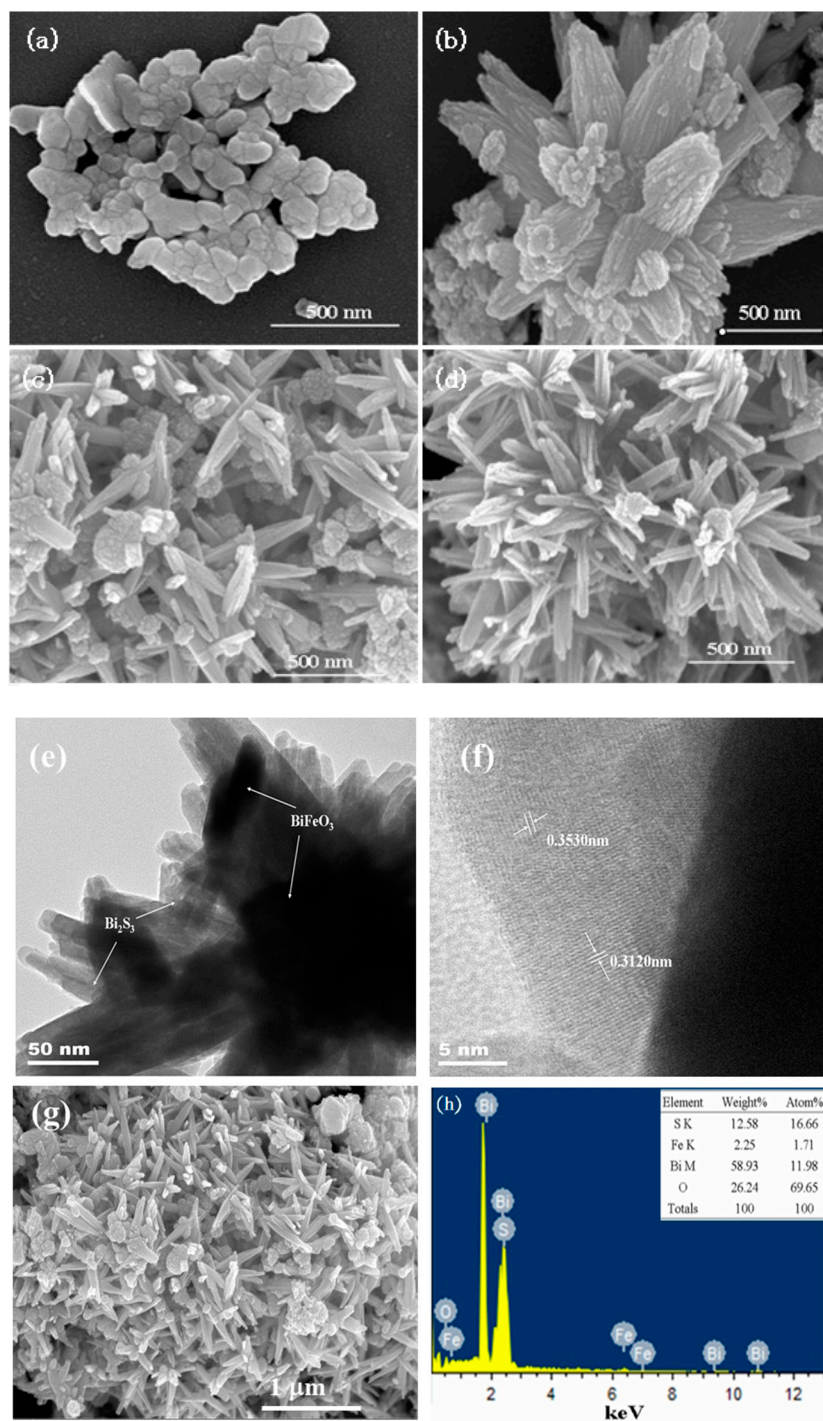


Figure 2. SEM images of samples (a) $BiFeO_3$; (b) $Bi_2S_3/BiFeO_3(1:4)$; (c) $Bi_2S_3/BiFeO_3(1:3)$; (d) $Bi_2S_3/BiFeO_3(1:2)$; (e) TEM of $Bi_2S_3/BiFeO_3(1:3)$; (f) HRTEM of $Bi_2S_3/BiFeO_3(1:3)$; (g) the selected area of the EDX; (h) the EDX spectrum of the $Bi_2S_3/BiFeO_3(1:3)$.

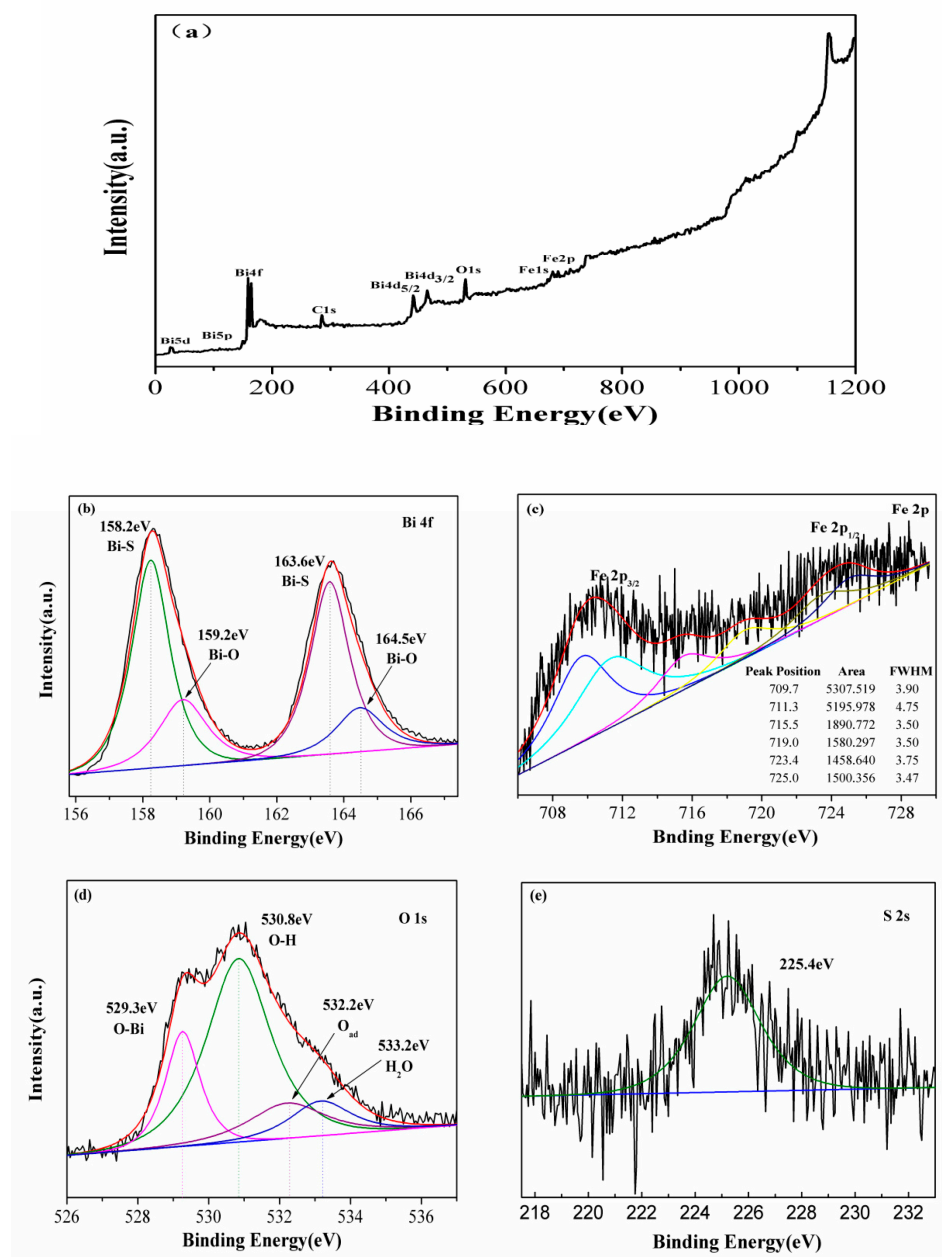


Figure 3. (a) Whole XPS spectra; (b) Bi(4f); (c) Fe(2p); (d) O(1s) and (e) S(2s) lines of the Bi₂S₃/BiFeO₃.

Photocurrent measurements were conducted for both pure BiFeO₃ and various molar ratios of Bi₂S₃/BiFeO₃, to probe electronic interactions, as depicted in Figure 4a. The composite materials exhibited markedly higher photocurrent responses compared to single BiFeO₃ during on–off cycles under visible-light irradiation. This enhancement can be directly attributed to the improved separation efficiency of photo-generated electrons within the heterojunction. Notably, when the molar mass ratio of Bi₂S₃/BiFeO₃ is 1:3, the photocurrent response surpassed that of the other ratios, signifying superior performance in charge separation. This enhanced photocurrent in the Bi₂S₃/BiFeO₃ heterojunction indicates heightened efficiency in separating electron–hole pairs, thereby enhancing the photocatalytic properties. To delve further into the charge separation process, electrochemical impedance spectroscopy (EIS) was employed. In EIS, a smaller arc radius signifies more effective separation of photo-generated electron–hole pairs and faster interface charge transfer.

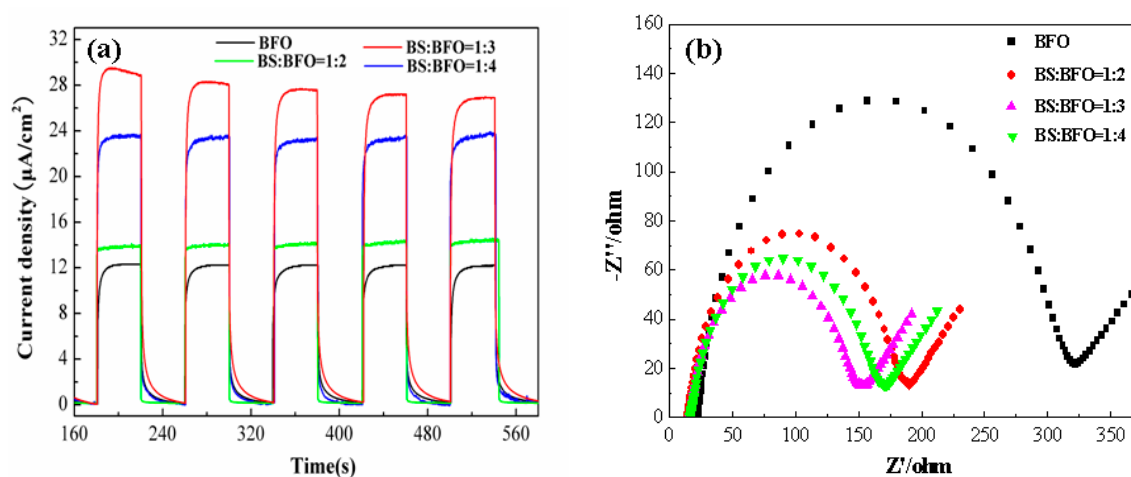


Figure 4. Photocurrents (a) BiFeO₃ and the proportions of Bi₂S₃ and BiFeO₃ ([Na₂SO₄] = 0.5 M) and (b) electrochemical impedance spectroscopy (EIS) for BiFeO₃ and the proportions of Bi₂S₃ and BiFeO₃ ([Na₂SO₄] = 0.5 M, [K₄Fe(CN)₆•3H₂O] = 2.5 mM, [K₃[Fe(CN)₆]] = 2.5 mM).

Figure 4b illustrates the fact that the arc radius of the Bi₂S₃/BiFeO₃ heterojunction is notably smaller than that of single BiFeO₃. This difference is particularly pronounced when the ratio of Bi₂S₃/BiFeO₃ is 1:3, where the arc radius is minimized. These results underscore the significant role played by the Bi₂S₃/BiFeO₃ heterojunction in improving the separation of photogenerated electron–hole pairs and facilitating efficient charge transfer at the interface. Consequently, the utilization of light energy is greatly enhanced, contributing to the overall photocatalytic efficiency.

The UV-Vis DRS spectra of the Bi₂S₃/BiFeO₃ heterojunction photocatalysts, with varying proportions, along with pure BiFeO₃, are presented in Figure 5. These spectra offer valuable insights into the optical properties of the materials. The optical absorption spectra, as revealed by DRS, demonstrate distinct characteristics. The pure BiFeO₃ sample exhibits intrinsic semiconductor-like absorption, primarily in the orange region of the visible spectra. In contrast, the Bi₂S₃/BiFeO₃ heterojunction composite materials exhibit absorption across the entire visible region of the spectrum, indicating enhanced light absorption capabilities. Notably, pure BiFeO₃ shows an absorption edge at approximately 610 nm, corresponding to a band gap of 2.03 eV for BiFeO₃. In the case of the Bi₂S₃/BiFeO₃ heterojunction, the absorption edge shifts towards the visible light region with increased intensity, compared to BiFeO₃. This shift signifies the photosensitization effect of Bi₂S₃ on BiFeO₃, where Bi₂S₃ enhances the absorption of visible light by the composite material. These findings emphasize the significant role of Bi₂S₃ in expanding the spectral range of light absorption by the BiFeO₃ photocatalyst, thereby enhancing its photocatalytic potential.

The photocatalytic activity of the Bi₂S₃/BiFeO₃ heterojunction with varying proportions of Bi₂S₃ was investigated through the photodegradation of the organic pollutant MG, as illustrated in Figure 6a. In the absence of the catalyst, the rate of photodegradation of MG under visible light ($\lambda > 420$ nm) irradiation remained below 40% within 2 h. However, when the Bi₂S₃/BiFeO₃ heterojunction catalysts were introduced, notable improvements were observed. MG was completely photodegraded after 60 min, demonstrating the enhanced photocatalytic efficiency of these materials. The photocatalytic performance followed the following order: Bi₂S₃/BiFeO₃ (1:3) > Bi₂S₃/BiFeO₃ (1:2) > Bi₂S₃/BiFeO₃ (1:4) > BiFeO₃. In particular, Bi₂S₃/BiFeO₃ (1:3) exhibited the highest photocatalytic efficiency, with approximately 99% of MG molecules decomposed within 60 min under visible light. This result underscores the significance of the optimal proportion between BiFeO₃ and Bi₂S₃ for enhanced photocatalytic activity. Scanning electron microscopy revealed that Bi₂S₃/BiFeO₃ (1:3) possessed a more uniform morphology, further supporting the superior photocatalytic performance observed. Moreover, full-wavelength scanning in Figure 6b highlights the degradation process: as MG was degraded by the addition of the Bi₂S₃/BiFeO₃ photocat-

alyst, the UV–visible absorption peak gradually weakened until it disappeared. During this weakening, there was a noticeable blue shift in the UV–visible absorption peak, indicating the generation of intermediate products in the optical degradation process, which, however, did not impede the degradation process. These findings underscore the substantial photocatalytic advantage of the $\text{Bi}_2\text{S}_3/\text{BiFeO}_3$ heterojunction, particularly when the proportion is optimized, and the importance of uniform particle surfaces in enhancing photocatalytic activity.

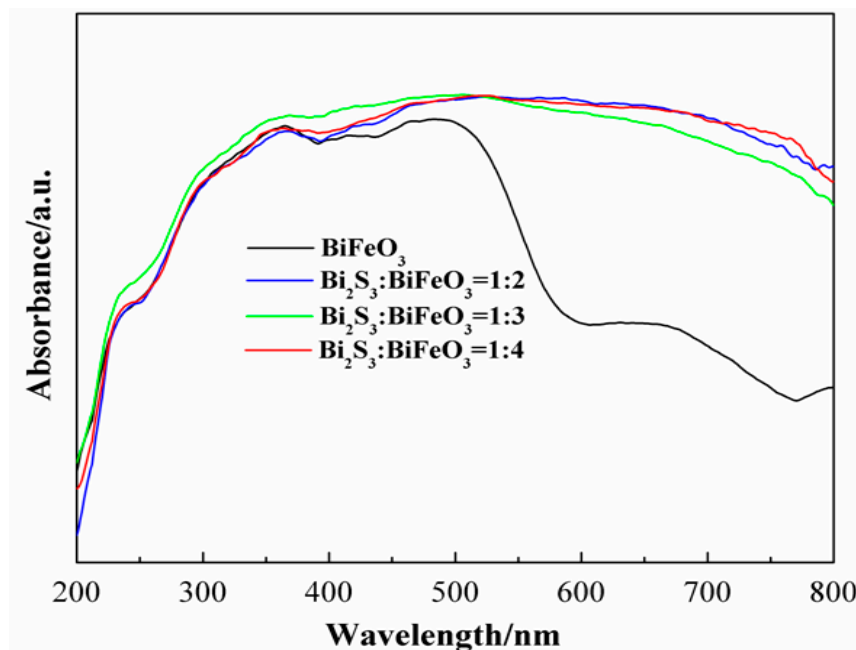


Figure 5. UV-vis diffuse reflection spectra of pure BiFeO_3 and the different proportions of $\text{Bi}_2\text{S}_3/\text{BiFeO}_3$.

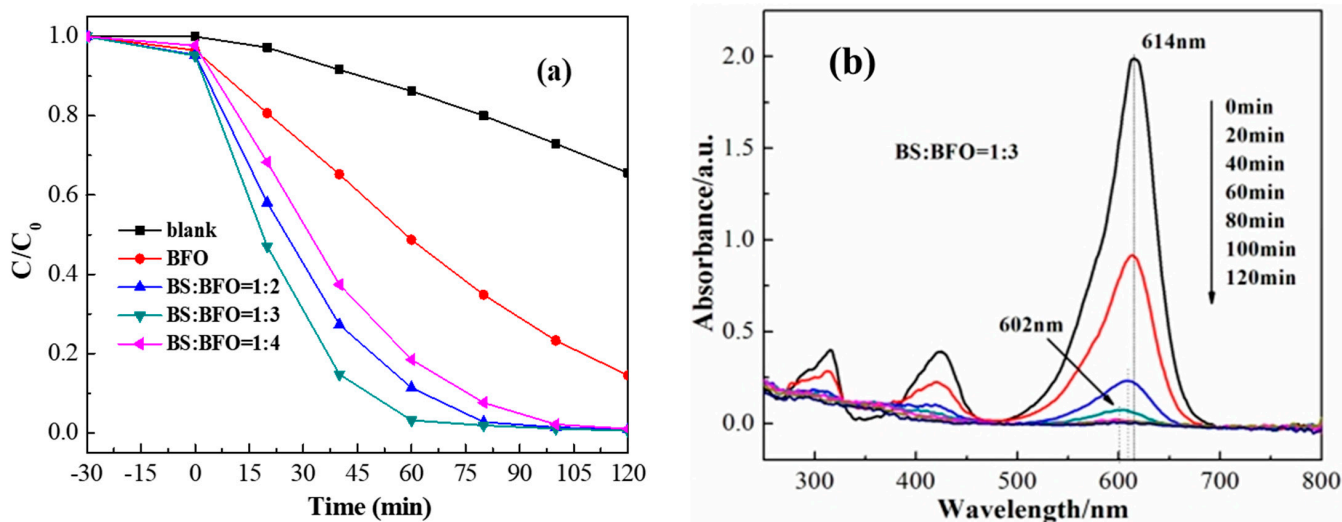


Figure 6. (a) Photocatalytic degradation of MG under visible-light irradiation using $\text{Bi}_2\text{S}_3/\text{BiFeO}_3$ heterojunctions as the catalyst; (b) the full-wavelength scanning of $\text{Bi}_2\text{S}_3/\text{BiFeO}_3(1:3)$ heterojunction photocatalyst.

As shown in Figure 7a, $\text{Bi}_2\text{S}_3/\text{BiFeO}_3(1:3)$ shows pH-dependent photocatalytic activity toward MG degradation, where the heterojunction catalyst exhibits excellent catalytic activity, with a pH around 6. An acidic or alkaline condition brings a negative effect toward

MG degradation, which may be attributed to the fact that the heterojunction catalyst is not stable enough against acid or alkaline corrosion. We also investigate the influence of catalyst dosage on the MG photo degradation, and the results are shown in Figure 7b. It is easy to find that, with the increase in the amount of catalyst used, the catalytic activity of heterojunctions toward MG degradation increases, which may be attributed to the increased catalyst amount, which could provide a more active side for oxygen activation to generate more reactive oxygen species. It should be noted here that an excess amount of catalyst would bring a light shading effect, which may bring negative effects toward pollutant removal. As can be seen from Figure 7b, limited activity improvement is found with the amount of catalyst increasing from 75 mg to 100 mg, and we believe that further increasing the amount of catalyst would not bring much improvement in catalytic activity. Thus, we then chose 100 mg of catalyst as the optimized condition to carry out other experiments.

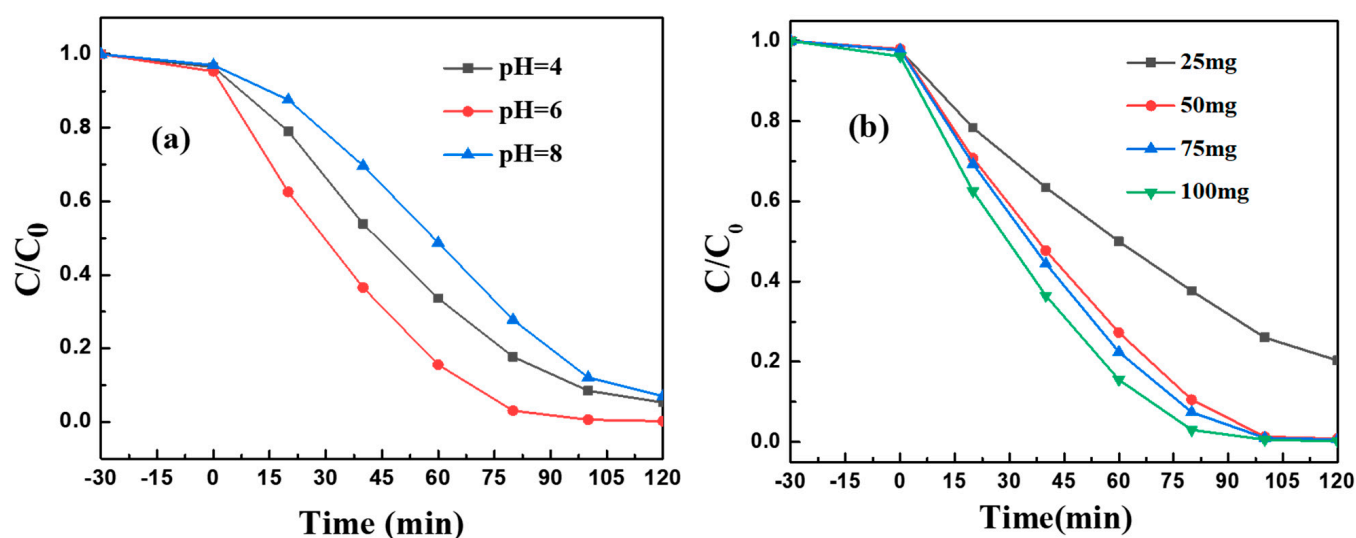


Figure 7. Photocatalytic performance of Bi₂S₃/BiFeO (1:3) toward MG degradation at (a) various pH conditions. (b) Effects of catalyst dosage on MG degradation.

To gain a deeper understanding of the photodegradation mechanism, various sacrificial agents were introduced to elucidate the roles of specific reactive groups in the reaction process. As depicted in Figure 8, when isopropanol (IPA) was introduced as a sacrificial agent to capture hydroxyl ($\bullet\text{OH}$) radicals, the degradation of MG was almost negligible. This observation suggests that $\bullet\text{OH}$ radicals play a crucial role in the degradation process, as they are potent oxidants, capable of effectively oxidizing many organic pollutants. Conversely, when triethanolamine (TEOA) was added to capture the photo-generated holes (h^+), and 4-benzoquinone (BQ) was used to capture $\bullet\text{O}_2^-$ radicals, the efficiency of MG degradation was significantly reduced. This reduction was particularly pronounced in the presence of TEOA. These results imply that, during the photodegradation reaction, $\bullet\text{O}_2^-$ radicals and photo-generated holes (h^+) work in tandem to facilitate the degradation of organic pollutants. The $\bullet\text{OH}$ radical, being a robust oxidant capable of oxidizing a wide range of organic pollutants, is likely a key contributor to the degradation process. These findings align with the existing literature, further supporting the significance of $\bullet\text{OH}$ radicals in the photodegradation of organic pollutants.

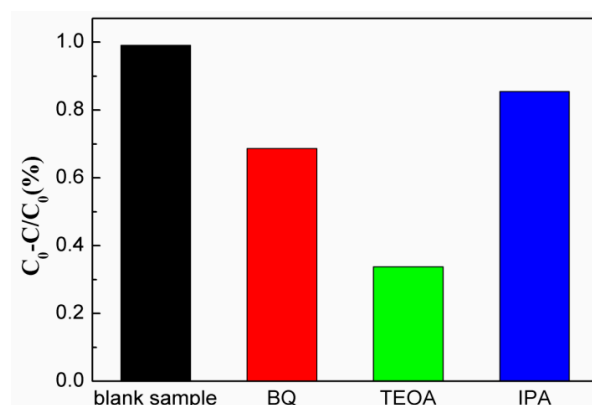
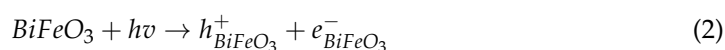
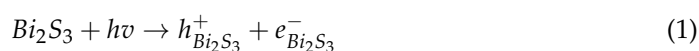


Figure 8. Effects of various scavengers on the photocatalytic efficiencies of Bi₂S₃/BiFeO₃ in MG degradation under visible-light irradiation.

To provide further authentication of the photocatalytic mechanisms at play, several key energy levels and oxidation–reduction potentials were considered (Figure 9). The band gap of BiFeO₃ was determined to be 2.05 eV, based on UV-Vis DRS spectra. Additionally, the conduction band of BiFeO₃ is at +0.21 eV ($E_{CB} = +0.21$ eV) [45], and the valence band is at +2.26 eV ($E_{VB} = +2.26$ eV). In contrast, Bi₂S₃ has a conduction band at 0V ($E_{CB} = 0$ V) [46] and a valence band at +1.38 eV ($E_{VB} = +1.38$ eV) [47]. Notably, the conduction band of Bi₂S₃ is more negative than that of BiFeO₃. Based on the above energy-band structure analysis, the photogenerated electrons are transferred from the conduction band of Bi₂S₃ to the conduction band of BiFeO₃, due to the more negative conduction band of Bi₂S₃. This facilitates the generation of $\bullet O_2^-$ on the material surface by oxygen absorption, which can then directly oxidize the target contaminant MG. On the other hand, the oxidation–reduction potential of $\bullet OH$ is 2.38 V [48], significantly more positive than the valence band of BiFeO₃ ($E_{VB} = +2.26$ V) [49] and Bi₂S₃ ($E_{VB} = +1.38$ eV) [50]. Consequently, the photoexcited Bi₂S₃/BiFeO₃ generates holes that are unable to oxidize water to form hydroxyl radicals. Furthermore, the valence band energy of Bi₂S₃ is lower than that of BiFeO₃. Thus, the photogenerated holes in the valence band of BiFeO₃ are transferred to the valence band of Bi₂S₃. This energy transfer enables the direct oxidation of MG. Considering the properties of each substance in the reaction system, these insights suggest the procedures and mechanisms of the reaction [50].



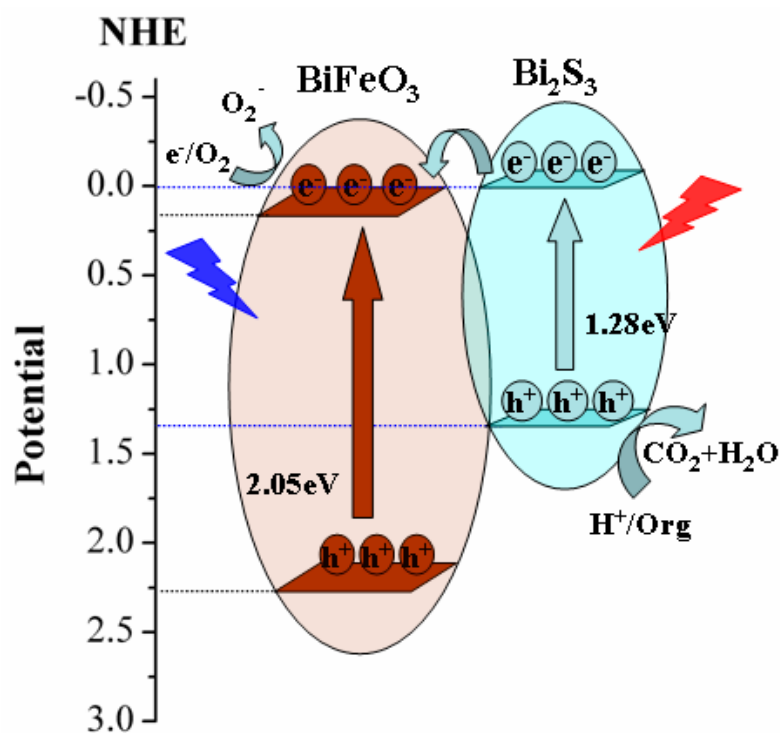


Figure 9. Schematic illustration of the $\text{Bi}_2\text{S}_3/\text{BiFeO}_3$ photocatalytic reaction process under visible-light irradiation.

3. Experimental

3.1. Material Synthesis

BiFeO_3 was prepared according to the reported method, with some modification [51]. Typically, 5 mM of bismuth nitrate pentahydrate ($\text{Bi}(\text{NO}_3)_3 \cdot 5\text{H}_2\text{O}$) and 5 mM of ferric nitrate ($\text{Fe}(\text{NO}_3)_3 \cdot 9\text{H}_2\text{O}$) were added into 35 mL of ethylene glycol monomethyl ether, to form a fine mixture. The solution was vigorously stirred until it reached a state of homogeneity, resulting in a transparent and stable solution at room temperature. Subsequently, the sample was left to dry for 24 h at 80 °C, yielding a gel-like powder. This powder was then carefully ground and subjected to heating in a muffle furnace at 550 °C for 4 h. After the heating process, the sample was allowed to cool to room temperature, and its final form was obtained through additional grinding.

Following this initial preparation, the next step involved the synthesis of $\text{Bi}_2\text{S}_3/\text{BiFeO}_3$ through an in situ growth process on the BiFeO_3 substrate under hydrothermal conditions, as depicted in Figure 10.

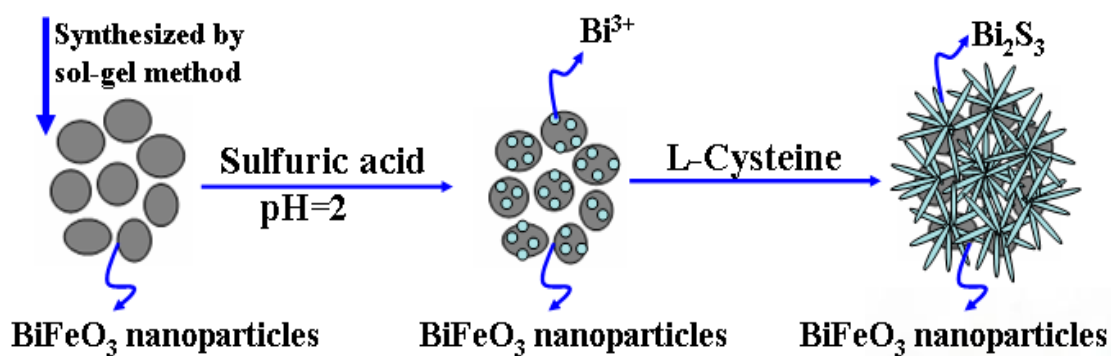


Figure 10. Schematic illustration of the $\text{Bi}_2\text{S}_3/\text{BiFeO}_3$ synthetic processes.

Commencing with three clean beakers, each received 35 mL of deionized water. Sequentially, L-cysteine was introduced at concentrations of 6 mM, 4 mM, and 3 mM into the respective beakers. Complete dissolution of L-cysteine was ensured. Sulfuric acid was employed to carefully adjust the pH level to 2, while maintaining precision in this process. With meticulous care, an equivalent quantity of BiFeO₃ (4 mM) was gradually added to each solution. Stirring continued until the BiFeO₃ was uniformly dispersed within the mix. This stirring process endured for an additional 30 min. The mixed solutions were then carefully transferred to a 50 mL autoclave. The autoclave was subjected to a hydrothermal reaction at 150 °C for a duration of 12 h. Following completion of the reaction, the contents underwent filtration, and the resulting material was thoroughly washed with deionized water and absolute ethanol. The Bi₂S₃/BiFeO₃ heterojunction materials obtained from the process were dried at 80 °C for 12 h under ambient air conditions. The final samples were categorized as Bi₂S₃/BiFeO₃ (1:2), Bi₂S₃/BiFeO₃ (1:3), and Bi₂S₃/BiFeO₃ (1:4), respectively, based on the ratios used during their preparation.

3.2. Characterization

The crystalline phase of the samples was investigated using X-ray diffraction (XRD, D8 Advance, Bruker, Mannheim, Germany), using graphite monochromatized Cu-K α ($\lambda = 1.5406 \text{ \AA}$) radiation at 40 kv and 40 mA with a scan rate of 2 °/min between 10° and 70°. The UV–vis diffuse reflectance spectra (DRS) of the powders were collected using a U-3900/3900H UV-vis spectrophotometer (UV-vis DRS, U-3900/3900H, Hitachi High-Technologies, Tokyo, Japan) equipped with an integrating sphere attachment. The general morphologies and micro-area chemical analysis of the samples were obtained using scanning electron microscopy images (SEM, Sirion 200, FEI, Eindhoven, The Netherlands) and energy-dispersive X-ray spectroscopy (EDS) with a scanning voltage of 5.00 kV. Further microstructure and crystallinity of the sample was analyzed using transmission electron microscopy (TEM, Tecnai F20, FEI, Hillsboro, OR, USA) and high-resolution transmission electron microscopy (HRTEM) observation. The chemical states of as-prepared photocatalysts were tested using monochromated Al-K α X-ray photoelectron spectroscopy (XPS, Axis Ultra DLD) at a residual gas pressure of less than 10^{−8} Pa.

Electrochemical measurements were performed on a CHI 660D electrochemical workstation (Shanghai Chenhua, Shanghai, China) by using a standard three-electrode system with a working electrode. (The working electrode was prepared by dip-coating on a 3 cm × 1 cm fluorine tin oxide (FTO) glass electrode, with the films drying under room condition.) A graphite electrode was used as the electrodes, and a standard calomel electrode in saturated KCl was used as a reference electrode. A total of 0.5 M sodium sulfate was used as the electrolyte solution for the photocurrent test, and 0.5 M sodium sulfate, 2.5 mM of potassium ferricyanide and potassium ferrocyanide were adopted as the supporting electrolyte for Ac impedance.

3.3. Photocatalytic Activity Evaluation

The effectiveness of the Bi₂S₃/BiFeO₃ heterojunction catalysts in photocatalysis was assessed through the degradation of Malachite Green oxalate (MG) under visible light conditions ($\lambda > 420 \text{ nm}$). These photocatalytic reactions were conducted using simulated solar light with an intensity equivalent to 300 W, generated by a Xe-lamp system from Asahi Spectra Co., Ltd. (Torrance, CA, USA) The initial concentration of the Malachite Green solution was set at 20 mg/L. The photocatalytic procedure was performed in a homemade reactor with catalytic conditions quite similar to the reported method; typically, 0.1 g of the catalyst was dispersed into 100 mL of the Malachite Green oxalate (MG) solution [52]. To establish a balance between the adsorption and desorption of Malachite Green on the catalyst surface, the mixture was magnetically stirred for 30 min in the dark.

At specified irradiation time intervals, approximately 5 mL of the suspension was extracted every 10 min. These samples were subsequently centrifuged to obtain clear solutions, which were then analyzed using a UV–vis spectrophotometer (UV-vis DRS, U-

3900/3900H, Hitachi High-Technologies, Tokyo, Japan). The maximum absorbance of the solution was determined at 614 nm. To provide a basis for comparison, parallel experiments using pure BiFeO₃ were conducted alongside the Bi₂S₃/BiFeO₃ experiments, allowing for an evaluation of the relative performance of Bi₂S₃/BiFeO₃, compared to pure BiFeO₃.

4. Conclusions

In summary, we have shown the first instance of fabricating nanoflower-shaped Bi₂S₃/BiFeO₃ heterojunctions via a simple sol–gel process. The formed type II heterojunction is found capable of providing a powerful built-in field to accelerate electron–hole spatial separation, which leads to the enhanced reactive oxygen species generation. As a result, the as-prepared Bi₂S₃/BiFeO₃ heterojunctions exhibit excellent photocatalytic performance toward MG degradation, where more than 99% of MG is removed within 2 h of photocatalysis. The innovative design shown in this work may offer new viewpoints in designing highly efficient photocatalysts for environmental purification. For real water purification, however, we still need to immobilize the catalyst, so as to prevent catalyst loss. The immobilization of the as-prepared Bi₂S₃/BiFeO₃ on a light-weight carrier, for example loofah, to construct floating materials, is another possibility for its practical application.

Author Contributions: Conceptualization, L.Z.; Methodology, R.Z. and P.Z.; Validation, L.Z.; Formal analysis, R.Z.; Investigation, R.Z. and P.Z.; Data curation, R.Z. and L.Z.; Writing—original draft, R.Z. and X.T.; Writing—review & editing, X.T. and Z.Z.; Supervision, X.T. and Z.Z.; Project administration, X.T.; Funding acquisition, X.T. All authors have read and agreed to the published version of the manuscript.

Funding: This work was financially supported by the National Natural Science Foundation of China (No. 52060019 and 22276087), the Key Project of Jiangxi Provincial Natural Science Foundation (No. 20202ACBL204015), the Key Research and Development Project of Jiangxi Province (No. 20212BBG73030).

Institutional Review Board Statement: Not applicable.

Informed Consent Statement: Not applicable.

Data Availability Statement: Data are contained within the article.

Conflicts of Interest: The authors declare no conflict of interest.

References

1. Zeng, Z.; Fan, Y.; Quan, X.; Yu, H.; Chen, S.; Zhang, S. Energy-transfer-mediated oxygen activation in carbonyl functionalized carbon nitride nanosheets for high-efficient photocatalytic water disinfection and organic pollutants degradation. *Water Res.* **2020**, *177*, 115798. [[CrossRef](#)]
2. Fung, C.-M.; Er, C.-C.; Tan, L.-L.; Mohamed, A.R.; Chai, S.-P. Red phosphorus: An up-and-coming photocatalyst on the horizon for sustainable energy development and environmental remediation. *Chem. Rev.* **2022**, *122*, 3879–3965. [[CrossRef](#)]
3. Li, S.; Lin, Y.H.; Zhang, B.P.; Wang, Y.; Nan, C.W. Controlled fabrication of BiFeO₃ uniform microcrystals and their magnetic and photocatalytic behaviors. *J. Phys. Chem. C* **2010**, *114*, 2903–2908. [[CrossRef](#)]
4. Gao, F.; Chen, X.Y.; Yin, K.B.; Dong, S.; Ren, Z.F.; Yuan, F.; Yu, T.; Zou, Z.G.; Liu, J.M. Visible-Light Photocatalytic Properties of Weak Magnetic BiFeO₃ Nanoparticles. *Adv. Mater.* **2007**, *19*, 2889–2892. [[CrossRef](#)]
5. Yang, X.; Zhang, Y.; Xu, G.; Wei, X.; Ren, Z.; Shen, G.; Han, G. Phase and morphology evolution of bismuth ferrites via hydrothermal reaction route. *Mater. Res. Bull.* **2013**, *48*, 1694–1699. [[CrossRef](#)]
6. Wang, X.; Lin, Y.; Ding, X.; Jiang, J. Enhanced visible-light-response photocatalytic activity of bismuth ferrite nanoparticles. *J. Alloys Compd.* **2011**, *509*, 6585–6588. [[CrossRef](#)]
7. Zhang, J.; Gondal, M.A.; Wei, W.; Zhang, T.; Xu, Q.; Shen, K. Preparation of room temperature ferromagnetic BiFeO₃ and its application as an highly efficient magnetic separable adsorbent for removal of Rhodamine B from aqueous solution. *J. Alloys Compd.* **2012**, *530*, 107–110. [[CrossRef](#)]
8. Xian, T.; Yang, H.; Dai, J.F.; Wei, Z.Q.; Ma, J.Y.; Feng, W.J. Photocatalytic properties of BiFeO₃ nanoparticles with different sizes. *Mater. Lett.* **2011**, *65*, 1573–1575. [[CrossRef](#)]
9. He, J.; Guo, R.; Fang, L.; Dong, W.; Zheng, F.; Shen, M. Characterization and visible light photocatalytic mechanism of size-controlled BiFeO₃ nanoparticles. *Mater. Res. Bull.* **2013**, *48*, 3017–3024. [[CrossRef](#)]
10. Liu, Z.; Qi, Y.; Lu, C. High efficient ultraviolet photocatalytic activity of BiFeO₃ nanoparticles synthesized by a chemical coprecipitation process. *J. Mater. Sci. Mater. Electron.* **2010**, *21*, 380–384. [[CrossRef](#)]

11. Soltani, T.; Entezari, M.H. Photolysis and photocatalysis of methylene blue by ferrite bismuth nanoparticles under sunlight irradiation. *J. Mol. Catal. A Chem.* **2013**, *377*, 197–203. [[CrossRef](#)]
12. Mohan, S.; Subramanian, B. A strategy to fabricate bismuth ferrite (BiFeO₃) nanotubes from electro spun nanofibers and their solar light-driven photocatalytic properties. *RSC Adv.* **2013**, *3*, 23737–23744. [[CrossRef](#)]
13. Zhang, X.; Liu, H.; Zheng, B.; Lin, Y.; Liu, D.; Nan, C.W. Photocatalytic and magnetic behaviors observed in BiFeO₃ nanofibers by electrospinning. *J. Nanomater.* **2013**, *2013*, 917–948. [[CrossRef](#)]
14. Guo, R.; Fang, L.; Dong, W.; Zheng, F.; Shen, M. Enhanced photocatalytic activity and ferromagnetism in Gd Doped BiFeO₃ nanoparticles. *J. Phys. Chem. C* **2010**, *114*, 21390–21396. [[CrossRef](#)]
15. Zhang, Z.; Liu, H.; Lin, Y.; Wei, Y.; Nan, C.W.; Deng, X. Influence of La Doping on Magnetic and Optical Properties of Bismuth Ferrite Nanofibers. *J. Nanomater.* **2012**, *2012*, 238605. [[CrossRef](#)]
16. Feng, Y.N.; Wang, H.C.; Luo, Y.D.; Shen, Y.; Lin, Y.H. Ferromagnetic and photocatalytic behaviors observed in Ca-doped BiFeO₃ nanofibers. *J. Appl. Phys.* **2013**, *113*, 146101. [[CrossRef](#)]
17. Li, S.; Zhang, J.; Kibria, M.G.; Mi, Z.; Chaker, M.; Ma, D.; Nechache, R.; Rosei, F. Remarkably enhanced photocatalytic activity of laser ablated Au nanoparticle decorated BiFeO₃ nanowires under visible-light. *Chem. Commun.* **2013**, *49*, 5856–5858. [[CrossRef](#)]
18. Schultz, A.M.; Zhang, Y.; Salvador, P.A.; Rohrer, G.S. Effect of Crystal and Domain Orientation on the Visible-Light Photochemical Reduction of Ag on BiFeO₃. *ACS Appl. Mater. Inter.* **2011**, *3*, 1562–1567. [[CrossRef](#)]
19. Niu, F.; Chen, D.; Qin, L.; Zhang, N.; Wang, J.; Chen, Z.; Huang, Y. Facile Synthesis of Highly Efficient p–n Heterojunction CuO/BiFeO₃ Composite Photocatalysts with Enhanced Visible-Light Photocatalytic Activity. *ChemCatChem* **2015**, *7*, 3279–3289. [[CrossRef](#)]
20. Zhang, Y.; Schultz, A.M.; Salvador, P.A.; Rohrer, G.S. Spatially selective visible light photocatalytic activity of TiO₂/BiFeO₃ heterostructures. *J. Mater. Chem.* **2011**, *21*, 4168–4174. [[CrossRef](#)]
21. Zhu, A.; Zhao, Q.; Li, X.; Shi, Y. BiFeO₃/TiO₂ Nanotube Arrays Composite Electrode: Construction, Characterization, and Enhanced Photoelectrochemical Properties. *ACS Appl. Mater. Interfaces* **2014**, *6*, 671–679. [[CrossRef](#)] [[PubMed](#)]
22. Li, T.; Shen, J.; Li, N.; Ye, M. Hydrothermal preparation, characterization and enhanced properties of reduced graphene–BiFeO₃ nanocomposite. *Mater. Lett.* **2013**, *91*, 42–44. [[CrossRef](#)]
23. Li, Z.; Shen, Y.; Guan, Y.; Hu, Y.; Lin, Y.; Nan, C.W. Bandgap engineering and enhanced interface coupling of graphene–BiFeO₃ nanocomposites as efficient photocatalysts under visible light. *J. Mater. Chem. A* **2014**, *2*, 1967–1973. [[CrossRef](#)]
24. Pineda, E.; Nicho, M.E.; Nair, P.K.; Hu, H. Optoelectronic properties of chemically deposited Bi₂S₃ thin films and the photovoltaic performance of Bi₂S₃/P₃OT solar cells. *Sol. Energy* **2012**, *86*, 1017–1022. [[CrossRef](#)]
25. Cao, J.; Xu, B.; Lin, H.; Luo, B.; Chen, S. Novel Bi₂S₃-sensitized BiOCl with highly visible light photocatalytic activity for the removal of rhodamine B. *Catal. Commun.* **2012**, *26*, 204–208. [[CrossRef](#)]
26. Cheng, H.; Huang, B.; Qin, X.; Zhang, X.; Dai, Y. A controlled anion exchange strategy to synthesize Bi₂S₃ nanocrystals/BiOCl hybrid architectures with efficient visible light photoactivity. *Chem. Commun.* **2012**, *48*, 97–99. [[CrossRef](#)] [[PubMed](#)]
27. Chen, P.; Gu, L.; Cao, X. From single ZnO multipods to heterostructured ZnO/ZnS, ZnO/ZnSe, ZnO/Bi₂S₃ and ZnO/Cu₂S multipods: Controlled synthesis and tunable optical and photoelectrochemical properties. *CrystEngComm* **2010**, *12*, 3950–3958. [[CrossRef](#)]
28. Calva-Yanez, J.C.; Rincon, M.E.; Solís de la Fuente, M.; Alvarado-Tenorio, G. Structural and photoelectrochemical characterization of MWCNT-TiO₂ matrices sensitized with Bi₂S₃. *J. Solid State Electrochem.* **2013**, *17*, 2633–2641. [[CrossRef](#)]
29. Jana, A.; Bhattacharya, C.; Datta, J. Enhanced photoelectrochemical activity of electro-synthesized CdS-Bi₂S₃ composite films grown with self-designed cross-linked structure. *Electrochim. Acta* **2010**, *55*, 6553–6562. [[CrossRef](#)]
30. He, H.; Berglund, S.P.; Xiao, P.; Chemelewski, W.D.; Zhang, Y.; Mullins, C.B. Nanostructured Bi₂S₃/WO₃ heterojunction films exhibiting enhanced photoelectrochemical performance. *J. Mater. Chem. A* **2013**, *1*, 12826–12834. [[CrossRef](#)]
31. Ata, S.; Shaheen, I.; Aslam, H.; Mohsin, I.U.; Alwadai, N.; Al Huwayz, M.; Iqbal, M.; Younas, U. Barium and strontium doped La-based perovskite synthesis via sol-gel route and photocatalytic activity evaluation for methylene blue. *Results Phys.* **2023**, *45*, 106235. [[CrossRef](#)]
32. Jiao, S.; Zhao, Y.; Bi, M.; Bi, S.; Li, X.; Wang, B.; Li, C.; Dong, Y. Removal of Methylene Blue from Water by BiFeO₃/Carbon Fibre Nanocomposite and Its Photocatalytic Regeneration. *Catalysts* **2018**, *8*, 267. [[CrossRef](#)]
33. Tseng, W.J.; Lin, R.D. BiFeO₃/α-Fe₂O₃ core/shell composite particles for fast and selective removal of methyl orange dye in water. *J. Colloid Interface Sci.* **2014**, *428*, 95–100. [[CrossRef](#)]
34. Qin, K.; Zhao, Q.; Yu, H.; Xia, X.; Li, J.; He, S.; Wei, L.; An, T. A review of bismuth-based photocatalysts for antibiotic degradation: Insight into the photocatalytic degradation performance, pathways and relevant mechanisms. *Environ. Res.* **2021**, *199*, 111360. [[CrossRef](#)] [[PubMed](#)]
35. Song, S.; Xing, Z.; Zhao, H.; Li, Z.; Zhou, W. Recent advances in bismuth-based photocatalysts: Environment and energy applications. *Green Energy Environ.* **2023**, *8*, 1232–1264. [[CrossRef](#)]
36. *JCPDS 20-0169*; Elements of X-ray Diffraction, B. D. Cullinitty, 2nd ed., Addison-Wesley, Reading, MA, 1978. JCPDS (Joint Committee on Powder Diffraction Standards): Newtown Square, PA, USA, 2023.
37. Dai, Y.; Wang, Y.; Yao, J.; Wang, Q.; Liu, L.; Chu, W.; Wang, G. Phosgene-Free Synthesis of Phenyl Isocyanate by Catalytic Decomposition of Methyl N-Phenyl Carbamate over Bi₂O₃ Catalyst. *Catal. Lett.* **2008**, *123*, 307–316. [[CrossRef](#)]

38. Zeng, Z.; Ye, F.; Deng, S.; Fang, D.; Wang, X.; Bai, Y.; Xiao, H. Accelerated organic pollutants mineralization in interlayer confined single Pt atom photocatalyst for hydrogen recovery. *Chem. Eng. J.* **2022**, *444*, 136561. [[CrossRef](#)]
39. Lu, X.; Pu, F.; Xia, Y.; Huang, W.; Li, Z. Facile fabrication of porous thin films of Bi₂O₃/Bi₂S₃ nanocomposite semiconductors at gas/liquid interface and their photoelectrochemical performances. *Appl. Surface Sci.* **2014**, *299*, 131–135. [[CrossRef](#)]
40. Wang, N.; Zhu, L.; Wang, M.; Wang, D.; Tang, H. Sono-enhanced degradation of dye pollutants with the use of H₂O₂ activated by Fe₃O₄ magnetic nanoparticles as peroxidase mimetic. *Ultrason. Sonochem.* **2010**, *17*, 526–533. [[CrossRef](#)]
41. Jiang, J.; Zou, J.; Anjum, M.N.; Yan, J.; Huang, L.; Zhang, Y.; Chen, J. Synthesis and characterization of wafer-like BiFeO₃ with efficient catalytic activity. *Solid State Sci.* **2011**, *13*, 1779–1785. [[CrossRef](#)]
42. Zhong, Y.; Shi, J.; Li, K.; Guo, H.; Yan, L.; Zeng, Z. Silicotungstic acid as electron transfer mediator in Z-scheme g-C₃N₄/H₄SiW₁₂O₄₀/Ag₃PO₄: Accelerated charge interface transportation for high-efficient photocatalysis. *Process Saf. Environ.* **2023**, *171*, 188–199. [[CrossRef](#)]
43. Xiao, H.; Zhang, Q.; Ahmad, M.; Dong, S.; Zhang, Y.; Fang, D.; Wang, X.; Peng, H.; Lei, Y.; Wu, G.; et al. Carbonate mediated hole transfer boosting the photocatalytic degradation of organic pollutants over carbon nitride nanosheets. *Sep. Purif. Technol.* **2023**, *306*, 122580. [[CrossRef](#)]
44. Marchon, B.; Carrazza, J.; Heinemann, H.; Somorjai, G.A. TPD and XPS studies of O₂, CO₂, and H₂O adsorption on clean polycrystalline graphite. *Carbon* **1988**, *26*, 507–514. [[CrossRef](#)]
45. Xu, W.; Fang, J.; Chen, Y.; Lu, S.; Zhou, G.; Zhu, X.; Fang, Z. Novel heterostructured Bi₂S₃/Bi₂Sn₂O₇ with highly visible light photocatalytic activity for the removal of rhodamine B. *Mater. Chem. Phys.* **2015**, *154*, 30–37. [[CrossRef](#)]
46. Humayun, M.; Zada, A.; Li, Z.; Xie, M.; Zhang, X.; Qu, Y.; Raziq, F.; Jing, L. Enhanced visible-light activities of porous BiFeO₃ by coupling with nanocrystalline TiO₂ and mechanism. *Appl. Catal. B Environ.* **2016**, *180*, 219–226. [[CrossRef](#)]
47. Li, X.; Ye, F.; Zhang, H.; Ahmad, M.; Zeng, Z.; Wang, S.; Wang, S.; Gao, D.; Zhang, Q. Ternary rGO decorated W₁₈O₄₉ @g-C₃N₄ composite as a full-spectrum-responded Z-scheme photocatalyst for efficient photocatalytic H₂O₂ production and water disinfection. *J. Environ. Chem. Eng.* **2023**, *11*, 110329. [[CrossRef](#)]
48. Kong, L.; Jiang, Z. Unusual reactivity of visible-light-responsive AgBr-BiOBr heterojunction photocatalysts. *J. Catal.* **2012**, *293*, 116–125. [[CrossRef](#)]
49. Bard, A.J.; Faulkner, L.R. *Electrochemical Methods: Fundamental and Application*; John Wiley & Sons: New York, NY, USA, 1980.
50. Li, X.; Zhu, J. Comparative study on the mechanism in photocatalytic degradation of different-type organic dyes on SnS₂ and CdS. *Appl. Catal. B Environ.* **2012**, *123–124*, 174–181. [[CrossRef](#)]
51. Xu, M.L.; Lu, M.; Qin, G.Y.; Wu, X.M.; Yu, T.; Zhang, L.N.; Li, K.; Cheng, X.; Lan, Y.Q. Piezo-Photocatalytic Synergy in BiFeO₃@COF Z-Scheme Heterostructures for High-Efficiency Overall Water Splitting. *Angew. Chem. Int. Ed.* **2022**, *61*, e202210700. [[CrossRef](#)]
52. Tang, J.; Wang, R.; Liu, M.; Zhang, Z.; Song, Y.; Xue, S.; Zhao, Z.; Dionysiou, D.D. Construction of novel Z-scheme Ag/FeTiO₃/Ag/BiFeO₃ photocatalyst with enhanced visible-light-driven photocatalytic performance for degradation of norfloxacin. *Chem. Eng. J.* **2018**, *351*, 1056–1066. [[CrossRef](#)]

Disclaimer/Publisher's Note: The statements, opinions and data contained in all publications are solely those of the individual author(s) and contributor(s) and not of MDPI and/or the editor(s). MDPI and/or the editor(s) disclaim responsibility for any injury to people or property resulting from any ideas, methods, instructions or products referred to in the content.